Fostering crack deviation via local internal stresses in Al/NiTi composites and its correlation with fracture toughness

Lv Zhao[a,*], Lipeng Ding[a,b], Jeroen Soete[c], Hosni Idrissi[a,b], Greet Kerckhofs[a,c], Aude Simar[a]

[a] *Institute of Mechanics, Materials and Civil Engineering, UCLouvain, Louvain-la-Neuve, Belgium*
[b] *EMAT, University of Antwerp, Antwerp, Belgium*
[c] *Department of Materials Engineering, KU Leuven, Leuven, Belgium*

Abstract

In the framework of metal matrix composites, a research gap exists regarding tailoring damage mechanisms. The present work aims at developing an Al/NiTi composite incorporating internal stresses in the vicinity of reinforcements. The composite is manufactured by friction stir processing which allows a homogenous NiTi distribution and a good Al/NiTi interface bonding. The internal stresses are introduced via shape memory effect of the embedded NiTi particles. The induced internal strain field is confirmed by digital image correlation and the corresponding stress field is evaluated by finite element simulation. It is found that the damage mechanism is modified in the presence of internal stresses. The consequent enhancement of fracture toughness arises by the fact that the internal stresses foster discrete damages shifted from the fracture ligament line. These damages release the stress concentration at the main crack tip and lead to a deviated crack path when coalescing to accommodate fracture propagation.

Keywords: Metal-matrix composites (MMCs), shape memory effect, damage mechanics, fracture toughness

1. Introduction

Mechanical strength is one of the key parameters in the design of metal-based structures in automotive and aerospace applications. In order to improve the mechanical properties of light metals such as aluminium and magnesium, a widely practiced and well documented approach consists of alloying with additional elements to form nanometric precipitates. The precipitates serve to hinder the dislocation movement and thus contribute to strengthening. Another possible strategy to strengthen alloys is adding reinforcement agents into metallic matrices to form metal matrix composites (MMCs) [1, 2, 3]. This can enable tailoring both functional [4] and mechanical properties [5, 6].

The improvement in mechanical strength is attractive in MMCs. The ductility sacrifice, however, remains a challenging issue due to the prevailing failure at the interface between the matrix and the reinforcements [7, 8]. Premature interface failure may also significantly decrease the fracture toughness

*corresponding author: lv.zhao@uclouvain.be

of the composite. It has additionally been widely recognized that metallic reinforcements allow creating stronger bonding than ceramic ones. However, the formation of brittle intermetallic phases at the metal-metal interface still degrades the material ductility [9]. The detrimental effect of embrittlement could be remedied in the first place by reducing the size and volume fraction of the reinforcements [10, 11]. Nevertheless, this remedy may impose a compromise on the desired content of reinforcements.

In the designs of MMCs, most of the previous efforts have simply pursued high mechanical strength, while little attention was paid to the crack growth mechanism [12] and fracture toughness [13]. Conversely, in the framework of another composite family based on ceramic matrices, a variety of designs were developed to toughen brittle materials involving generally low fracture resistance [14, 15]. The toughening effect was mainly achieved via internal thermal stresses resulting from the mismatch in thermal expansion coefficients. The introduction of thermal stresses was first practiced in dual phase ceramic materials [16, 17] and then transferred to ceramic matrix composites (CMCs) incorporating secondary particles [14, 15]. The underlying mechanism of toughness improvement in CMCs consists of repelling and deviating the crack tip by compressive internal stresses [15]. Indeed, in brittle materials, crack deviation involves one of the most efficient approaches to improve the fracture toughness, given that more energy should be dissipated to create new surfaces. Successful examples can be found in bioinspired (nacre structure) ceramics [18, 19]. The strategy of increasing fracture toughness by crack deviation can also be applied to metallic materials. Recent modeling showed that the fracture toughness of ductile materials could be correlated to the crack deviation which was quantified by the fracture surface roughness [20, 21]. An increase in fracture surface roughness can be translated into an increase in fracture toughness.

A research gap still exists in the framework of MMCs in terms of toughening metallic matrices, in particular via crack deviation resulting from local internal stresses. Thermal internal stresses might not be a good solution to tackle this problem, since a large mismatch in thermal expansion coefficients necessitates ceramic reinforcements, while the use of metallic reinforcements needs cooling from high temperature, which will favor the formation of intermetallic phases and change the thermal state of the matrix material such as precipitate hardenable aluminium. Alternatively to thermal stresses, shape memory alloy (SMA) particles [22] offer a possibility to introduce local internal stresses in MMCs. These internal stresses are obtained via the shape change of the embedded SMA reinforcements, using the shape memory effect [23, 24]. In literature, NiTi particle reinforced composites have already been developed in non-heat treatable Al alloys [25, 26, 27] as well as precipitate hardenable Al alloys [9, 28]. In these studies, the authors mainly investigated the strengthening effect relative to internal stresses, while the fracture toughness was not assessed. It was surprisingly found that the internal stresses induced by SMA particles had no strengthening effect on the composite [25]. This could be explained by the fact that lo-

cal tension and compression internal stresses co-exist around each NiTi particle and the resultant global internal stress is null. Nevertheless, the internal stresses are expected to more effectively affect the crack initiation and propagation, in spite of the co-existence of tension and compression. The crack propagation, which develops from very local damage to the coalescence of local voids [29, 30], is supposed to be more sensitive to the local stress state.

The present work aims at achieving crack deviation, i.e., enhancing fracture toughness, via the introduction of internal stresses in ductile materials. For this purpose, an Al/NiTi composite is developed. Friction stir processing (FSP), a technique derived from friction stir welding (FSW) [31] is employed to manufacture the composite. This technique ensures solid-state of the material and thus hinders solidification defects and complex chemical reactions between the metal matrix and the reinforcements while resulting in solid interface bonding, as exerted in the pioneer studies on Al/NiTi composites manfactured by FSP [25] or electrical current assisted FSW [27]. Moreover, FSP has been proven to be an efficient technique to uniformly integrate reinforcement particles in MMCs [32, 33]. Following the composite manufacturing, internal stresses are generated by pre-straining and the shape recovery effect of the integrated NiTi particles. The induced internal strain field is confirmed using digital image correlation and the corresponding internal stress field is assessed by a finite element simulation. The crack propagation path is investigated with single edge pre-cracked tension tests and the fracture toughness is measured with compact tension tests. A correlation between fracture surface roughness and fracture toughness is finally established.

2. Experiments

2.1. Design of Al/NiTi composites

The Al/NiTi composite is designed according to the principle illustrated in Fig. 1. The first step consists of integrating NiTi particles inside the Al matrix and ensuring the martensitic phase of the embedded NiTi. It should be noted that martensitic and austenitic NiTi particles share the same external shape at stress-free state. Secondly, a pre-straining is conducted to change the shape of the embedded NiTi particles, involving a phase transformation from twinned martensite to detwinned martensite. Finally, a heating is applied to the composite to force the NiTi particles to recover their shape before the pre-straining step. This involves a phase transformation from detwinned martensite to austenite. Internal stresses are generated in the vicinity of NiTi particles since the surrounding Al matrix needs to accommodate the shape change of the NiTi during the aforementioned phase transformation. Theoretically, the internal stresses will be in tension on the two sides along the pre-straining direction and in compression on the sides perpendicular to the pre-straining direction (Fig. 1, after heating).

2.2. Materials

In order to evade complex reactions between the reinforcement and the alloying elements in Al alloys, and to avoid severe defects such as particle clustering and cavities due to inappropriate material flow involved in high strengh Al alloy based MMCs [34, 35], the commercial pure aluminium 1050-H14 was selected as the composite matrix. The chemical composition is displayed in Table 1. The Al plate is 200 mm long, 80 mm wide and 6 mm thick. The NiTi particles used in this study present a nearly equiatomic composition. The particles have an almost spherical shape (see Supplementary Fig. 1). The mean particle diameter is 79 μm according to a granulometric measurement. The phase transformation temperatures of the NiTi particles were measured using differential scanning calorimetry (DSC) from -80 °C to 80 °C at a rate of 2 °C min^{-1}. The transformation temperature values were found as A_s=30 °C, A_f=45 °C, and M_s=15 °C, M_f=-10 °C (see Supplementary Fig. 2).

2.3. Composite manufacturing

The composite manufacturing process is schematically represented in Fig. 2. The integration of NiTi particles in the Al matrix was conducted by FSP. A groove, which is 166 mm long, 3 mm wide and 4.8 mm deep, was machined in the Al plate. The NiTi particles were embedded inside the groove and then covered with a 0.2 mm thick Al 1050 sheet. The cover sheet was used to impede the loss of NiTi particles during FSP. The backing plate and the clamping system were installed in a tank containing cutting oil, which helps to increase the cooling rate. FSP was conducted with a conventional milling machine, using a tool made of H13 steel that is composed of a scrolled shoulder of 20 mm in diameter and a M6 threaded Triflat pin of 5.2 mm in length (see Ref. [36] for a schematic view of the tool geometry). The tool was tilted backwards with an angle of 1°. During processing, the tool penetrated 5.4 mm into the material and then stirred the material with a rotational speed of 1000 rpm and a transverse speed of 50 mm/min. The relatively high rotational speed and low transverse speed were applied to generate sufficient heat to increase the material flow in the processed zone, thus to favor the dispersion of NiTi particles. Four passes were performed to ensure a uniform distribution of the reinforcements. The phase transformation temperatures of the composite with integrated NiTi particles were shown to be almost identical as those of the as-received NiTi powder (see Supplementary Fig. 2).

After FSP, the plate was first machined to eliminate the cover sheet as well as the FSP burrs, the thickness of the composite plate was thus reduced to 5 mm. Then the plate was cooled down to -20 °C for 24 hours to obtain the martensitic phase of the NiTi particles. Afterwards, the plate was cold rolled, reducing the thickness from 5 mm to 3 mm (a reduction of 40%) to pre-strain the NiTi particles (Fig. 1). Note that this thickness reduction is expected to be sufficient to generate detwinned martensite in the NiTi particles, given that the shape memory effect induced internal strain has been detected after pre-straining the Al1100/NiTi composites through a thickness reduction of 38% [25]. The cold rolled plate was finally

heat treated at 80 °C during 15 minutes to recover the shape of the NiTi particles, which results from the martensite to austenite transformation. Further study was conducted to confirm the presence of the shape memory effect induced internal strain, see section 2.4.2.

In order to assess the mechanical properties of the Al/NiTi composite, two additional reference materials were manufactured. The first one was subject to the same FSP and cold rolling processes without NiTi particles. It is referred to as FSPed Al. Note that the mechanical properties of the Al base material are not relevant in the present work, since FSP would significantly change the microstructure of the Al matrix via dynamic recrystallization [31]. The second one contained NiTi particles but the cold rolling was conducted with austenitic NiTi, i.e., suppressing the prior cooling as well as the following heating steps. Therefore, it does not present the shape memory effect and thus has no local internal stresses generated by the shape recovery of the NiTi particles. This material is named Al/NiTi-A composite. The manufacturing steps of the Al/NiTi composite and the two reference materials are summarized in Table 2. It is worth mentioning that the Al/NiTi-A should also contain internal stresses that are generated during cooling from FSP passes. This thermal stress field is anyhow also present in the Al/NiTi composite and thus will not be studied here. The present work exclusively focuses on the shape memory effect induced internal stresses.

2.4. Characterization

2.4.1. Microstructural characterization

The overview of the NiTi particle integration was addressed using a ZEISS FEGSEM Ultra 55 Scanning Electron Microscope (SEM). The spatial distribution of the NiTi particles was investigated with high resolution microfocus X-ray Computed Tomography (HR-microCT), using a Phoenix Nanotom S 180 kV μCT system from General Electric. Two sets of sample dimensions were addressed, both extracted in the FSP stir zone: 3×3×3 mm and 1×1×1 mm, resulting in voxel sizes of 2 μm and 0.8 μm, respectively. The larger sample was used to characterize the size distribution of the embedded NiTi particles, while the smaller sample was used to investigate the potential fragmentation of NiTi particles during FSP. The analysis of the HR-microCT datasets was performed in Avizo 9.5 (ThermoFisher Scientific). First, the particles were separated from the matrix by means of a contrast threshold function, which returned a binary version of the original gray-scale image. Voxels with gray-values below the chosen threshold were labeled as the matrix, while those above were labeled as the NiTi particles in the segmented image. Next, the overlapping NiTi particles in the binary images were separated by combining watershed, distance transform and numerical reconstruction algorithms. The particle objects consisting of only 3 voxels or less were filtered out in order to exclude noise and to avoid partial-volume effects, which, if not properly accounted for, can lead to erroneous determinations of feature dimensions and phase volume fractions. Finally, each NiTi particle was given a unique ID and the particle properties,

such as the particle equivalent diameter, the particle volume, the surface area, etc., were calculated. The interface between the NiTi particle and the Al matrix was analyzed with a FEI Tecnai G2 F20 Transmission Electron Microscope (TEM). The TEM samples were prepared using a dual-beam focused ion beam (FIB) instrument (FEI Helios Nanolab 650) across the interface. The sample size was about 5 μm × 3.5 μm × 100 nm. The microstructure observation below M_f was conducted with a Gatan 636 double-tilt cooling holder at -20 °C.

2.4.2. Shape memory effect induced internal strain

In order to confirm the presence of local internal stresses and to assess the strain field induced by the shape memory effect of the NiTi particles, Digital Image Correlation (DIC) was performed, using the matlab toolbox NCorr [37]. The surface morphology induced by chemical etching served as micro-scale speckle patterns for the image correlation. The DIC sample was extracted from the cold rolled composite, which was then mechanically polished to obtain a smooth surface. Finally a 30 minutes of OPS (colloidal silica) finishing was applied to induce a slight etching effect. A reference image was taken before heat treatment, using an Olympus opto-digital microscope. Subsequently, a deformed image was taken at the same position after heating the sample at 80 °C for 15 minutes. In order to validate the DIC measurement and evaluate the corresponding internal stress field, a finite element simulation mimicking the shape recovery of the NiTi particle in the Al matrix was conducted, as will be described in section 3.2.

2.4.3. Mechanical tests

A nano-indentation test, using a nano-indenter Agilent G200, was performed to investigate the possible matrix strengthening mechanism in the Al/NiTi composite. During the test, the hardness of the Al matrix in both the composite and the FSPed Al was measured. The indentation depth was set to 500 nm to avoid interactions with the NiTi particles. This relatively low depth would induce high hardness due to the size effect [38]. However, the nano-indentation was employed only for comparing the strength of the Al matrix between the Al/NiTi composite and the FSPed Al. The hardness was calculated from the recorded force versus indentation depth following the method of Oliver and Pharr [39]. The fit was carried out at the indentation depth range between 450 and 500 nm to minimize the size effect. Nine indentations were performed to assess the average hardness.

Uni-axial tensile tests and single edge pre-cracked tensile tests were performed to assess the mechanical strength and the crack propagation behavior, respectively. The geometry and dimension of the samples are shown in Supplementary Fig. 3. The pre-cracks were introduced with a razor blade. The tests were conducted in-situ inside the SEM using a micro-tensile machine (Gatan microtest tensile stage) to monitor the crack propagation process. The loading rate was 0.1 mm/min.

Compact tension tests were also performed to compare the fracture toughness of the Al/NiTi com-

posite with the two reference materials (Table 2). Two tests were performed for each material. The compact tension geometry is provided in Supplementary Fig. 4. The load was applied using a Zwick tensile (Zwick Z250) machine with a load rate of 0.2 mm/min. A clip-on gage (MTS model 632.02F-20) was used to measure the crack mouth opening distance. The effective crack length was determined by the unloading compliance method. The stress intensity factor under plane stress condition was evaluated according to the ASTM E561 standard, which is dedicated to thin compact tension specimens.

3. Results

3.1. Microstructure

A typical cross-section of the friction stir processed zone is shown in Fig. 3a. The distance between the two red dashed lines corresponds to the FSP tool pin size (6 mm). It can be noticed that the NiTi particles have been dispersed in a larger region than the pin stirring zone, due to the high material flow and the tool shoulder stirring effect. A uniform particle distribution is obtained after 4 passes, which can be observed in the 3D HR-microCT images, see Figs. 3b and c corresponding to voxel sizes of 2 μm and 0.8 μm, respectively. The volume fraction of NiTi reinforcements is about 6.7% according to the measurements with a voxel size of 2 μm.

When comparing the size distribution (volume-weighted) between the as-received NiTi powder (using laser granulometry with 0.375 μm as detection limit) and the embedded NiTi particles (2 μm HR-microCT data), as presented in Fig. 3d, it is found that the two distribution profiles match reasonably well. The average size is maintained after 4 passes of FSP (76 μm for embedded NiTi vs. 79 μm for as-received NiTi). Meanwhile, one can notice more particles smaller than 40 μm and less particles larger than 100 μm in the composite compared to the as-received powder. This could imply that some of the big reinforcements are fragmented under the thermomechanical effects of FSP. The 0.8 μm voxel size HR-microCT scan allowed analyzing the size distribution for particles smaller than 40 μm. The latter is illustrated in both number-weighted and cumulative volume-weighted ways, as presented in Fig. 3e. It is found that the smallest particle that has been identified has an equivalent diameter of 2.2 μm, which is close to the detection limit (1.4 μm) of the 0.8 μm CT scan, considering a threshold of 3 voxels volume. The small NiTi particles are numerous, their volume occupation is, however, very low, as reflected by the comparison of the two distribution profiles in Fig. 3e. It is worth mentioning that no NiTi particles smaller than 1.5 μm in diameter have been identified by SEM analysis. This means that the 0.8 μm HR-microCT scan can be considered appropriate for assessing the volume-weighted particle size distribution.

According to SEM observations at large magnification (×10K), uniformly distributed Fe-rich intermetallic particles, which are typical impurities in aluminium alloys [40], are present both in the Al matrix

of the FSPed Al and in the vicinity of NiTi particles in the Al/NiTi composite (Figs. 3f and g, respectively). SEM-EDX (Energy dispersive X-ray) analysis also confirms their composition as Fe-rich (insert of Fig. 3f). Most of the Fe-rich particles have sub-micron sizes, due to the strong stirring of FSP [41]. The average spacing between the Fe-rich particles is around 0.8 μm in both the FSPed Al and the Al/NiTi composite, according to a 2D nearest neighbor distance analysis, based on the particle centroids that were observed with SEM. A 3D distribution analysis would require a sub-micron resolution (100 nm achieved by Synchrotron radiations [41]), but this Fe-rich particle distribution is not critical in the present work, and is thus not further assessed.

FSP also causes the grain size reduction in the aluminium matrix. As can be noticed in Fig. 3g and 4b, the grain size is typically around 1 μm after 4 passes of FSP in both the FSPed Al and Al/NiTi composite, note that the average grain size of the as-received Al was 80 μm. The presence of the NiTi particles does not allow further refining the grains of the Al matrix since a large size of second phase particles has a negligible Zener pinning effect [42], note that the NiTi particles (76 μm) are much larger than the Al grains (1 μm) in the composite.

The TEM analysis at the Al/NiTi interface is presented in Fig. 4. Fig. 4a shows a low magnification bright field TEM (BF-TEM) image of the cross-sectional FIB thin foil prepared on a single Al/NiTi interface, preselected inside the FIB/SEM dual beam instrument. The BF-TEM image of Fig. 4b shows the presence of sub-grain boundaries within the Al grains. Moreover, a Fe-rich particle can be observed in the Al matrix, as confirmed by TEM-EDX. The morphology and size of the Fe-rich particle correspond well to SEM observations presented in Figs. 3f and g. Regarding the Al/NiTi interface, an intermetallic (IM) layer is observed in the BF-TEM image (Fig. 4c). According to the TEM-EDX analysis (Table 3) as well as the nano beam diffraction (inset of Fig. 4c), the intermetallic has been identified as Al_3Ti (tetragonal structure). The mean thickness of the IM layer is about 50 nm, which is much smaller than that obtained in powder metallurgy manufactured Al/NiTi composites (larger than 1 μm) [9]. The IM layer is formed mainly by the diffusion from the Al matrix to the NiTi particle, which might explain why the interface between the NiTi particle and intermetallic layer is smoother. High resolution TEM observation of the interface between the IM layer and the Al matrix shows a good interface bonding (Fig. 4d). The interface bonding is of paramount importance in the present study, since it ensures the load transfer that is required for the shape memory induced internal strain in the Al matrix. In addition, a good bonding is expected to relieve the ductility reduction due to the presence of hard reinforcements. The diffusion of Ni and Ti from the NiTi particles into the Al matrix is investigated using TEM-EDX analysis. The analyzed area is represented by the red dashed box in Fig. 4a and the chemical composition is presented in Table 3. It is found that the analyzed region contains 0.81 at.% Ni and 0.30 at.% Ti, which is much higher than the theoretical solid solubility of Ni and Ti in Al matrix. The presence of Ni and

Ti is further confirmed by the TEM-EDX spectrum, as shown in Fig. 4e. The relatively high content of dissolved Ni and Ti can be explained by the fact that the high dislocation density in the Al matrix next to the NiTi particle reduces the chemical potential and increases the solid solubility. This effect has already been documented in literature [43, 44].

3.2. Shape memory effect

The internal strain field in relation to the shape recovery of the NiTi particles is assessed by DIC. Fig. 5 shows the two images used for DIC computation as well as the obtained strain maps. When comparing the surface morphologies of the Al matrix before and after heat treatment, some deformation bands in the vicinity of the NiTi particle can be observed after triggering the shape memory effect (arrows in Fig. 5b). These deformation bands are more clearly translated into an internal strain field by the DIC analysis. Figs. 5c and d display the strain fields in the cold rolling direction (RD) and the normal direction (ND), respectively. In the RD, tension is dominant at the left and right sides of the NiTi, accompanied by compression at the top and bottom as counterpart. In the ND, compression dominates at the top and bottom sides of the NiTi, while tension in other places accommodates equilibrium. The obtained strain field is in good agreement with the expected response of the shape memory effect, knowing that the cold rolling flattens the NiTi particles in the normal direction while elongates them in the rolling direction. It is worth mentioning that the observed deformation bands and the corresponding internal strain are not generated by the heat treatment, considering the relatively low temperature (80°C) used in the treatment.

The DIC measurements only allow studying the internal strain field around the reinforcement. In order to assess the corresponding internal stress field, shape recovery of NiTi particle was mimicked with finite element modeling (FEM). A spherical NiTi particle embedded inside an Al matrix was modeled with the commercial finite element software Abaqus 2016 [45]. Isotropy is assumed in the modeling. The NiTi particle with a diameter of 100 μm has following elastic properties assigned: E = 80 GPa, Poisson's ratio = 0.4. The Young's modulus is taken as the average of two values reported for austenitic NiTi polycrystal presenting random grain orientation distribution, i.e. 82 GPa in [23] and 78.6 GPa in [46]. The Al matrix has a cubic shape of 1x1x1 mm (Fig. 6a) and following mechanical properties assigned: E = 69 GPa, Poisson's ratio = 0.33, yield strength σ_y = 112 MPa, strain hardening $\sigma = 132\varepsilon_p^{0.02}$. The plastic strain hardening behavior was obtained from a fit of a uni-axial tensile test on the FSPed Al (see Supplementary Fig. 5). The whole model was meshed with 3D elements C3D8R. The far Al matrix involves an element size of 50 μm while the particle is meshed with an element size of 5 μm (Fig. 6a). The two mesh sizes are accommodated by a transition zone in the vicinity of the particle. The shape recovery of the NiTi particle is realized by imposing an initial stress inside the particle and releasing this stress in a static calculation step. A compression stress of -400 MPa and a tensile stress of 800 MPa are applied in the particle along the compression direction (ND) and the rolling direction (RD), respectively.

Thus, the particle expands in the compression direction while it retracts in the rolling direction during the establishment of a new equilibrium between the particle and the matrix, mimicking the shape recovery of the NiTi reinforcement. The initial stress level is set to match the order of magnitude of the strain as well as strain field shape, as measured by DIC. It sounds reasonable that the applied initial tensile stress is higher than the compression one, because the shape memory performance of the NiTi is better in tension than in compression, as reported in literature [47].

The simulation results are shown in Figs. 6b-f. In order to be comparable with the DIC measurement, where the correlation does not involve the edge of the NiTi particle, the elements (size of 5 μm) containing the NiTi edge in the model are not displayed in the results. A direct comparison of strain values in both the RD and the ND between the DIC measurement and the FEM result is presented in Fig. 6b. The values are extracted along cross lines that coincide with the major and minor axes of the NiTi particle. The distance to the particle edge is normalized with the particle size. It can be noticed that the FEM reproduces reasonably well the shape recovery induced local strain that is measured by DIC. The discrepancy is likely related to the fact that the NiTi particle, despite general spherical shape, involves local shape irregularity, for instance the right side close to the particle has a sharp edge while the left side is more flat (see Fig. 5). Regarding the strain field, the arrangement of tension and compression in the FEM result is in good agreement with that visualized by the DIC measurements (see Figs. 5c and 5d). In terms of stress field, tension is located on the left and right sides of the NiTi particle in the RD direction, while compression is found on the top and bottom of the particle in the ND direction. The largest stress components (155 MPa in the RD and -143 MPa in the ND) are much higher than the yield strength of the Al matrix (112 MPa). It is thus expected that damage first occurs at the left and right sides of the particles in the RD when subject to an external load. This will be discussed in section 3.5

3.3. Mechanical strength and ductility

The nanoindentation hardness of the Al matrix in both the Al/NiTi composite and the FSPed Al is given in Table 4. Indents in the Al/NiTi composite are sufficiently far from the NiTi particles so that the nanoindentation hardness of the Al matrix is not affected by the presence of the NiTi particles (see Supplementary Fig. 6). There is almost no strengthening in the Al matrix of Al/NiTi compared to the FSPed Al. However, according to the uni-axial tensile tests, as shown in Fig. 7 and Table 4, the Al/NiTi composite presents a 24 MPa increase in strength compared to the FSPed Al. This implies that the strengthening of Al/NiTi is related to the NiTi particles rather than the Al matrix. Both materials present a limited strain hardening capacity due to cold rolling. The yield strength and the ultimate tensile strength are thus almost identical. Note that the tensile curve of the Al/NiTi-A composite is not reported since the local internal stresses do not contribute to strengthening, as previously reported in literature [25]. Additional tensile tests on samples just after FSP (without either cold rolling or heat treatment at 80 °C)

also show that the presence of NiTi particles increases the ultimate tensile strength by 23 MPa (from 60 MPa to 93 MPa), i.e., identical to the strength increase after cold rolling and heat treatment at 80 °C (Table 4). This indicates that the strengthening in the Al/NiTi composite is not modified by cold rolling.

The higher strength in the Al/NiTi is accompanied by a lower ductility. The fracture strain is estimated from the sample section area before (A_0) and after (A_f) fracture, using Eq. 1. The larger scattering of the tensile properties in the Al/NiTi compared to the FSPed Al is attributed to slight variation in the volume fractions of reinforcement particles. A slightly larger NiTi content results in a higher mechanical strength but a lower ductility. It is observed that the FSPed Al involves a cup-cup feature, while the Al/NiTi a slant fracture surface, see Figs. 7b and c, respectively. The slant fracture surface can be attributed to the local shear damage around the NiTi particle, as indicated by the arrows in Fig. 7d. It should be noted that the shear damage takes place in the Al matrix (SEM-EDX mapping in the inset of Fig. 7d), close to the NiTi particle, rather than at the Al/NiTi interface. The local damages most likely initiate from the Fe-rich particles in the matrix. This is confirmed by the sheared dimples observed on the fracture surface, see Fig. 7e. Moreover, in the dimple-less region in Fig. 7e, a transgranular shearing of the Al grains can be noticed; the revealed grain size corresponds well to the grain size revealed by the TEM image (Figs. 4a and 4b).

$$\varepsilon_f = ln(\frac{A_0}{A_f}) \tag{1}$$

3.4. Crack path

The crack path is investigated with pre-cracked tension tests (see Supplementary Fig. 3b). The overviews of the pre-cracked samples prior to loading are shown in Figs. 8a-c for the FSPed Al, the Al/NiTi-A and Al/NiTi composites, respectively. Note that there were no fracture properties extracted from the pre-cracked sample state, meaning that the difference in pre-crack size is not taken into account here. The final fracture paths are presented in Figs. 8d-f, revealing a straight crack propagation in the FSPed Al while cracks deviate in the Al/NiTi-A and Al/NiTi composites.

Given that the sample thickness is relatively small (1.5 mm) and that plane stress condition is prevailing, the fracture path at the mid-thickness level, where the stress triaxiality is the highest [29, 30], should be more representative of the fracture process. Therefore, the fractured samples are polished to mid-thickness, and the fracture paths are visualized at that level in Fig. 9. It can be seen at this stage that the crack deviations at mid-thickness level in both the Al/NiTi-A and the Al/NiTi are more pronounced than those observed on the sample surface, while the crack path remains relatively straight in the FSPed Al. The crack deviation will be quantified later in Fig. 13. Moreover, the crack deviation in the Al/NiTi is related to the NiTi particles, and local crack branching can be noticed, as shown in Fig. 9c.

In order to assess the local fracture behavior during crack propagation, the fracture surfaces of the

FSPed Al and the Al/NiTi are studied with SEM and presented in Fig. 10. The fracture surface morphology of Al/NiTi-A is similar to that of Al/NiTi, and is provided in Supplementary Fig. 7. The dashed rectangles in Figs. 10a and d represent the initial sample thickness. The thickness reduction in the FSPed Al is much larger than that in the Al/NiTi composite. It means that during the crack propagation in the FSPed Al, the crack tip necking dissipates a significant amount of energy in the fracture process zone (FPZ), in contrast to the Al/NiTi composite. When focusing locally on the fracture surface of the FSPed Al, one can observe aligned dimples in the middle of the fracture surface. The dimples are traces of local voids that nucleated on the Fe-rich particles, which can eventually be noticed inside the dimples, see Fig. 10b. The dimple size and spacing are both around 1 μm (Fig. 10c). The fact that the dimples are confined in the middle of the fracture surface indicates that the crack propagates much faster inside the sample than on the sample surface. Regarding the local fracture behavior in the Al/NiTi composite, two populations of dimples can be observed. The larger dimples are related to the NiTi particles. At high magnification, one can observe a coverage of Al on the NiTi particle. The Al coverage has been confirmed by SEM-EDX mapping, as shown in Fig. 10e. The second population of dimples are related to fracturing or decohesion of Fe-rich particles [30, 48]. They are present not only in the interparticle matrix, but also on the NiTi surface, see Fig. 10f. These small dimples have very similar size and spacing compared to those observed on the fracture surface of FSPed Al (Fig. 10c). Their presence indicates that the crack propagation in the Al/NiTi is accommodated by void nucleation on Fe-rich particles at the vicinity of the NiTi particles, rather than interface decohesion between the Al matrix and the NiTi reinforcements.

3.5. Crack deviation mechanism with and without internal stresses

It has been shown that crack deviation emerges in the presence of NiTi particles, and it is more pronounced when local internal stresses introduced by the shape memory effect of NiTi are present (see Fig. 9). In order to understand the crack deviation mechanism, interrupted tensile tests have been carried out on both the Al/NiTi-A and the Al/NiTi composites. In-situ tensile tests are terminated after a given length of crack propagation and the samples are totally unloaded. The samples are then polished to mid-thickness level in order to assess the damage ahead of the crack tip. The crack in the Al/NiTi-A composite is presented in Fig. 11a. It can be seen that the main crack tip was deviating to bypass a NiTi particle upon unloading. No damage can be observed in the vicinity of the NiTi particles directly ahead of the main crack tip. However, regarding the Al/NiTi composite (Fig. 11b), local voids related to NiTi particles are observed ahead of the main crack tip. The largest void, which is also closest to the main crack tip, appears to be coalescing with the main crack tip upon termination of the test, while those further away from the crack tip are still in their growth stage.

Based on the aforementioned observations, the effects of NiTi particles as well as local internal

stresses on the crack propagation are proposed and illustrated in Figs. 11c and d. In the case of Al/NiTi-A (Fig. 11c), the crack propagates straight ahead in the Al matrix if no reinforcement particles are located right on or sufficiently close to the crack propagation path. The crack will bypass any NiTi particle located ahead of the crack tip. The bypass is operated by local damage nucleation and growth alongside of the NiTi particle and subsequently by the merging between the local damage and the main crack. This crack growth scenario has also been shown in microstructure-based simulation of fracture in Al/SiC composites, with and without particle fracture [12, 49]. In addition, the simulation showed that very slight crack deviation could be achieved by the bypass mechanism, which corresponds well to our experimental observation (Fig. 9b). In the case of Al/NiTi composite (containing local internal stresses from shape memory effect), micro-voids are first generated on Fe-rich intermetallics near the NiTi particles, since they are subject to a combined stress field incorporating concentrated stress at the main crack tip as well as the initial local tensile stress (generated by the shape memory effect of the NiTi particles). These micro-voids then grow and coalesce to larger local damages at the vicinity of the NiTi particles. The local damages finally coalesce with the main crack and control the crack propagation. Since the NiTi particles are randomly distributed in the Al matrix, the crack will deviate to reach the local damages.

3.6. Fracture toughness

Due to the thickness limitation, plane strain fracture toughness cannot be assessed in the present study. However, K_R measurements (ASTM E561 standard) can be performed with relatively thin compact tension samples, which offer a comparison of plane stress fracture toughness between the Al/NiTi and the two reference materials, i.e., the FSPed Al and the Al/NiTi-A. As the crack propagation on the sample surface is not fully representative of the real fracture process, the unloading compliance method has been applied to determine the physical crack length.

The loading curves and the K_R curves are presented in Figs. 12a and b, respectively. The Al/NiTi and the Al/NiTi-A present very close global strength, which is higher than that of the FSPed Al sample. The K_R values are plotted in function of the crack growth length which is obtained via the compliance of the sample at each unloading. It is worth mentioning that the calculated initial crack length is in good agreement with the measurement prior to loading, partly validating the quality of the measurement. The Al/NiTi composite presents the highest plane stress toughness (20.3±0.4 MPa.m$^{1/2}$), and the FSPed Al the lowest (18.4±0.1 MPa.m$^{1/2}$). The Al/NiTi-A yields an intermediate plane stress toughness (19.2±0.4 MPa.m$^{1/2}$). The aforementioned values are obtained with two tests for each material. Interestingly, after the crack mouth opening distance reaches the limit stroke of the clip-on gage (5 mm) for all the three materials, the crack growth in the FSPed Al is the smallest, although its fracture toughness is lowest. This can be explained by the fact that the crack tip necking in FSPed Al dissipates a large amount of energy

in the fracture process zone and can thus accommodate a large crack mouth opening, while slowing down the crack propagation inside the neck. In this sense, the difference in the real fracture dissipation between the FSPed Al and the two composites should be even larger. The crack deviation is supposed to be responsible for the higher toughness of Al/NiTi over Al/NiTi-A, albeit the mechanical strength is almost identical in both materials.

4. Discussion

4.1. Internal stresses in Al/NiTi composite

The concept of reinforcing metal matrices using shape memory alloys dated from the early 90s, initially investigated by numerical approaches [23, 24]. First experimental practices can be found in [50, 26], where powder metallurgy was used to manufacture composites. More recently, FSP was applied to embed shape memory particles in the aluminium matrix, and it was shown that FSP could improve the composite quality via a more uniform distribution of reinforcements and a cleaner interface between reinforcement and matrix [25, 28]. Among the former investigations, little efforts were made to highlight the internal stresses; only average stresses were evaluated by X-ray diffraction method [25]. However, it should be noted that the local internal stress field is the most distinguishable feature of shape memory alloy reinforced composites, it is therefore necessary to confirm its existence.

In the present work, the internal strain produced by the shape memory effect has been locally assessed via DIC and the corresponding internal stress field has been estimated by finite element simulations. DIC is suitable for the local strain field measurement in the Al/NiTi composite since the reference (FSP+cold rolling) and current (FSP+cold rolling+heat treatment) material states can be compared at the same local position. This is different from other approaches like X-ray diffraction or neutron diffraction which require a completely stress free material to obtain the reference, and most importantly cannot allow assessing the strain field at the fine scale (smaller than 100 μm) of the NiTi particle.

4.2. Strengthening mechanisms in Al/NiTi composite

The potential contributions to strengthening in the Al/NiTi composite are presented below:

$$\Delta\sigma = \Delta\sigma_{Orowan} + \Delta\sigma_{Hall-Petch} + \Delta\sigma_{\Delta CTE} + \Delta\sigma_{IS} + \Delta\sigma_{load} \tag{2}$$

$\Delta\sigma_{Orowan}$ denotes the Orowan strengthening [51], $\Delta\sigma_{Hall-Petch}$ stands for the grain boundary strengthening, $\Delta\sigma_{\Delta CTE}$ is attributed to increase in dislocation density resulting from thermal expansion mismatch in the composite, σ_{IS} accounts for the effect of internal stresses induced by the shape memory performance of NiTi. The last term, $\Delta\sigma_{load}$ represents the load bearing effect.

It should be noted that $\Delta\sigma_{Orowan}$ can be neglected in the present study since the NiTi reinforcements are much larger than the critical size for which the Orowan mechanism intervenes (generally smaller than 1 μm [52]). With regard to the Hall-Petch mechanism, the nanoindentation measurements (with an indent size about 3 times the grain size) show a very similar nanoindentation hardness in the FSPed Al and the inter-particle matrix in the Al/NiTi composite. This indicates the absence of strengthening resulting from grain refinement. Indeed, it has already been shown that the grain size in both the FSPed Al and the Al matrix of the composite is around 1 μm, see Fig. 3g and Fig. 4b. $\Delta\sigma_{IS}$ is expected to be a negligible contribution because of the co-existence of internal tension and compression around each NiTi particle (Fig. 5). This has been unraveled in [25].

The load bearing effect can be evaluated using the shear lag model proposed in [53]:

$$\Delta\sigma_{load} = 0.5 f_b \sigma_0 s \tag{3}$$

here, f_b represents the volume fraction of the reinforcements, σ_0 is the strength of the matrix, and s denotes the aspect ratio, which can be considered as 1 in the present work. The shear lag theory is originally used to analyze the yield strength, here it is applied to calculate the ultimate tensile strength since the two strengths are very close due to the extremely low strain hardening capacity, as discussed in section 3.3. Taking the tensile properties from Table 4 into account, one can notice that the load bearing would lead to a strengthening of 4 MPa, which is relatively low compared to the strength increase in the composite. It is worth mentioning that the shear lag model may not be fully valid for particulate reinforcements, but its application in the present work allows estimating the contribution from the load bearing effect which is, however, low and negligible (4 MPa). A 2D finite element simulation incorporating 7% of NiTi particles (diameter randomly varying from 40 to 100 μm) in the Al matrix (using the material properties described in section 3.2) reveals a strengthening of only 1 MPa, confirming again the very low load bearing contribution of particulate reinforcements.

In this sense, the strengthening is expected to be mainly attributed to the thermal induced dislocation loops around NiTi particles. The contribution $\Delta\sigma_{\Delta CTE}$ can be assessed by [54]:

$$\Delta\sigma_{\Delta CTE} = \sqrt{3}\beta G_m b \sqrt{\frac{12 f_p \Delta C.\Delta T}{b d_p}} \tag{4}$$

where G_m is the shear modulus of the matrix, b is the Burgers vector, f_b is the volume fraction of reinforcements as aforementioned, ΔC is the difference between the coefficient of thermal expansion of the matrix and the reinforcement, ΔT is the difference of the temperature reached in FSP and the room temperature, d_p is the equivalent diameter of the reinforcement, β is the product of the Taylor factor [55] and the strain-hardening constant taken as 0.5 [54]. Since the particle size in the Al/NiTi composite involves a large range, from 2.2 μm to 150 μm, $\Delta\sigma_{\Delta CTE}$ is first calculated for each sub-group of NiTi

particles with a size bin of 5 μm and then combined to yield the global strengthening [56], using

$$\Delta\sigma_{\Delta CTE} = \sqrt{(\Delta\sigma_{\Delta CTE}^{2.2-7.2\mu m})^2 + \Delta\sigma_{\Delta CTE}^{7.2-12.2\mu m})^2 + ...\Delta\sigma_{\Delta CTE}^{147.2-150\mu m})^2} \quad (5)$$

Considering a global volume fraction of 6.7% and the temperature reached in FSP as 90% of the melting point of the Al matrix, the obtained value is 10 MPa.

The total estimated strength increase is found to be lower than the experimentally obtained one. Therefore, the above analysis does not allow a full identification of the strengthening mechanisms in Al/NiTi composites. In fact, the solid solutions of Ni and Ti in the Al matrix (Fig. 4a and Table 3) can also play a role in the increase in mechanical strength. The contribution from these two solid solutions may not be well captured by the theoretical assessment, since they are distributed locally (around NiTi particles) and moreover associated with thermal mismatch induced dislocations. In this respect, the solute atoms of Ni and Ti strengthen the effect of thermal expansion mismatch via the fact that the solute atoms hinder the slip of the generated dislocations. We propose that the solid solution is partly responsible for the gap between the analytical and experimental mechanical strengths in the Al/NiTi composite. Certainly, the real strengthening mechanisms are complex and hard to be fully and accurately assessed by the simple analytical models employed in the present work.

4.3. Correlation between toughness and crack deviation

It has been shown that the Al/NiTi presents larger crack deviation and slightly higher fracture toughness than the Al/NiTi-A as well as the FSPed Al. In order to quantify the crack deviation and its relation to fracture toughness, a correlation function [21] is used to characterize the fracture surface roughness in the crack propagation direction. The correlation function $\Delta h(\delta x)$, is defined as:

$$\Delta h(\delta x) = \sqrt{< [h(x + \delta x) - h(x)]^2 >_x} \quad (6)$$

Here, $<>_x$ stands for the average value over x, the crack propagation direction. δx is a selected distance with which the typical difference of height along the crack path is calculated. The correlation function generally involves a power law with δx

$$\Delta h(\delta x) \propto \delta x^{\beta} \quad (7)$$

where β is the Hurst exponent. The measure of fracture surface roughness is the saturation value of the correlation function, Δh_s in a log-log plot of Δh vs. δx. The surface roughness is quantified with two samples of each type at mid-thickness. The values are then correlated with the fracture toughness from the compact tension tests, see Fig. 13. It is found that larger fracture surface roughness corresponds to higher fracture toughness, which is coherent with prior numerical investigations [21].

According to the correlation function assessment, the surface roughness is the largest for the Al/NiTi, followed by the Al/NiTi-A and the FSPed Al. In this respect, it can be concluded that the presence of NiTi particles provides a primary source of crack deviation. When the reinforcements are located on the crack propagation path, the crack will bypass these particles, resulting in a slightly deviating trajectory (see Fig. 11c). The crack deviation effect of the reinforcement particles is, however, limited. Particles shifted from the fracture ligament have a limited ability to attract and deviate the crack tip, in the case of good interface bonding. With regard to the Al/NiTi which incorporates internal stresses around the reinforcements, ”premature” damages occur at the vicinity of the embedded particles which can be located out of range of the expected crack path. These damages then grow, releasing the stress at the crack tip, and finally coalesce with the main crack tip, fostering a larger crack deviation (Fig. 11d) compared to the Al/NiTi-A. Nevertheless, it should be noted that even in the Al/NiTi composite, the first local damages arise from Fe-rich intermetallics, leading to ductile damage development. This should be differentiated from the case where a brittle or defective interface leads to large and uncontrollable damages, which is expected to have a negative impact on the fracture toughness. It is very important that the interface Al/NiTi is sufficiently bonded, as seems to be the case for the Al/NiTi composites in this study (Fig. 4d), thanks to the large plastic strain and limited heating of the FSP process.

5. Conclusions

An Al/NiTi composite that incorporates local internal stresses has been developed and characterized in both its microstructural and mechanical aspects. Special attention has been paid to the crack deviation assessment and the correlation between fracture toughness and fracture surface roughness. The following conclusions can be drawn:

1. A uniform distribution of NiTi particles is obtained in the composite manufactured by Friction Stir Processing (FSP). The 4-pass FSP leads to limited fragmentation of the embedded reinforcements. TEM observations show that interfacial product is limited to a very thin layer and good bonding is obtained.

2. Local internal stresses are produced using the shape memory effect of the NiTi particles, which has been evidenced through local strain by a DIC analysis and quantified by a finite element simulation. The obtained internal stress/strain field is in good agreement with the expected one generated from the shape recovery of the NiTi reinforcements.

3. The integration of relatively large NiTi particles (76 μm) via FSP leads to a 22% increase in ultimate tensile strength. The strengthening is mainly attributed to thermal mismatch induced dislocations, load bearing and solid solution of Ni and Ti in the Al matrix.

4. Crack deviation has been enhanced and correlated to a slight increase in fracture toughness in the Al/NiTi composite containing local stresses compared to the reference stress free Al/NiTi-A composite

and the FSPed Al. The deviation is driven by local internal stress controlled void nucleation, growth and coalescence.

Acknowledgment

This research work has been exclusively supported by the European Research Council (ERC) under the European Union's Horizon 2020 research and innovation program (grant agreement n°716678). The X-ray computed tomography facilities of the Department of Materials Engineering of the KU Leuven are financed by the Hercules Foundation. H. Idrissi is mandated by the Belgian National Fund for Scientific Research (FSR-FNRS). The authors acknowledge Professor F. Delannay from UCLouvain for fruitful discussions.

Declarations of interest: none

References

[1] N. Hansen, D. J. Jensen, T. Leffers, H. Lilholt, T. Lorenten, A. S. Pedersen, O. B. Pedersen, B. Ralph, Metal-matrix composites: processing, microstructure and properties, Risø National Laboratory, Denmark, 1991.

[2] T. W. Clyne, P. J. Withers, An introduction to metal matrix composites, Cambridge University Press, Cambridge, 1993.

[3] A. Mortensen, J. Llorca, Metal matrix composites, Annu. Rev. Mater. Res. 40 (2010) 243–270.

[4] Z. Tan, D. Xiong, G. Fan, Z. Chen, Q. Guo, C. Guo, G. Ji, Z. Li, D. Zhang, Enhanced thermal conductivity of diamond/aluminum composites through tuning diamond particle dispersion, J. Mater. Sci. 53 (2018) 6602–6612.

[5] M. Kouzeli, A. Mortensen, Size dependent strengthening in particle reinforced aluminium, Acta Mater. 50 (2002) 39–51.

[6] J. Liu, Z. Chen, F. Zhang, G. Ji, M. Wang, Y. Ma, V. Ji, S. Zhong, Y. Wu, H. Wang, Simultaneously increasing strength and ductility of nanoparticles reinforced Al composites via accumulative orthogonal extrusion process, Mater. Res. Lett. 6 (2018) 406–412.

[7] A. Mertens, A. Simar, J. Adrien, E. Maire, H. M. Montrieux, F. Delannay, J. Lecomte-Beckers, Influence of fibre distribution and grain size on the mechanical behaviour of friction stir processed Mg-C composites, Mater. Charact. 107 (2015) 125–133.

[8] A. Simar, A. Mertens, S. Ryelandt, F. Delannay, L. Brassart, Mean-field model analysis of deformation and damage in friction stir processed Mg-C composites, Mater. Sci. Eng. A 723 (47) (2018) 324–333.

[9] R. R. Thorat, D. D. Risanti, D. S. Martin, G. Garces, P. E. J. R. D. del Gastillo, S. van der Zwaag, On the transformation behavior of NiTi particulate reinforced AA2124 composites, J. Alloy. Compd. 477 (2009) 307–315.

[10] C. Nan, D. Clarke, The influence of particle size and particle fracture on the elastic/plastic deformation of matrix composites, Acta Mater. 44 (1996) 3801–3811.

[11] Z. Wang, M. Song, C. Sun, Y. He, Effect of particle size and distribution on the mechanical properties of SiC reinforced Al-Cu alloy composites, Mater. Sci. Eng. A 528 (2011) 1131–1137.

[12] A. Ayyar, N. Chawla, Microstructure-based modeling of crack growth in particle reinforced composites, Compos. Sci. Technol. 66 (2006) 1980–1994.

[13] A. Rabiei, L. Vendra, T. Kishi, Fracture behavior of particle reinforced metal matrix composites, Composites A 39 (2008) 294–300.

[14] G. C. Wei, P. F. Becher, Improvement in mechanical properties in SiC by addition of TiC particles, J. Am. Ceram. Soc. 67 (1984) 571–574.

[15] M. Taya, S. Hayashi, A. S. Kobayashi, H. S. Yoon, Toughening of a particulate-reinforced ceramic-matrix composite by thermal residual stress, J. Am. Ceram. Soc. 73 (1990) 1382–1391.

[16] W. D. Kingery, Note on thermal expansion and micro-stresses in two phase composites, J. Am. Ceram. Soc. 40 (1957) 351–352.

[17] R. M. Fulrath, Internal stresses in model ceramic systems, J. Am. Ceram. Soc. 42 (1959) 423–429.

[18] R. O. Ritchie, The conflicts between strength and toughness, Nat. Mater. 10 (2011) 817–822.

[19] F. Bouville, E. Maire, S. Meille, B. V. de Moortèle, A. J. Stervenson, S. Deville, Strong, tough and stiff bioinspired ceramics from brittle constituents, Nat. Mater. 13 (2014) 508–514.

[20] A. Srivastava, L. Ponson, S. Osovski, E. Bouchaud, T. Tvergaard, A. Needleman, Effect of inclusion density on ductile fracture toughness and roughness, J. Mech. Phys. Solids 63 (2014) 62–79.

[21] A. Srivastava, S. Osovski, A. Needleman, Engineering the crack path by controlling the microstructure, J. Mech. Phys. Solids 100 (2017) 1–20.

[22] K. Otsuka, X. Ren, Physical metallurgy of Ti-Ni-based shape memory alloys, Prog. Mater. Sci. 50 (2005) 511–678.

[23] Y. Yamada, M. Taya, R. Watanabe, Strenghtening of metal matrix composite by shape memory effect, Mater. Trans. JIM 34 (1993) 254–260.

[24] G. Q. Song, Q. P. Sun, Effect of microstructure on the mechanical behavior of NiTi shape memory alloy reinforced aluminum matrix composite, Smart Mater. Struct. 9 (2000) 693–700.

[25] M. Dixit, J. W. Newkirk, R. S. Mishra, Properties of friction stir-processed Al 1100-NiTi composite, Scr. Mater. 56 (2007) 541–544.

[26] G. A. Porter, P. K. Liaw, T. N. Tiegs, K. H. Wu, Fatigue and fracture behavior of nickel-titanium shape-memory alloy reinforced aluminium composites, Mater. Sci. Eng. A 314 (2001) 186–193.

[27] J. P. Oliveira, J. F. Duarte, P. Inácio, N. Schell, R. M. Miranda, T. G. Santos, Production of Al/NiTi composites by friction stir welding assisted by electrical current, Mater. Des. 113 (2017) 311–318.

[28] D. R. Ni, J. J. Wang, Z. N. Zhou, Z. Y. Ma, Fabrication and mechanical properties of bulk NiTip/Al composites prepared by friction stir processing, J. Alloy. Compd. 586 (2014) 368–374.

[29] T. Pardoen, F. Hachez, B. Marchioni, P. Blyth, A. G. Atkins, Mode I fracture of sheet metal, J. Mech. Phys. Solids 52 (2004) 423–452.

[30] A. Pineau, A. A. Benzerga, T. Pardoen, Failure of metals I: Brittle and ductile fracture, Acta Mater. 107 (2016) 424–483.

[31] R. S. Mishra, Z. Y. Ma, Friction stir welding and processing, Mater. Sci. Eng. R 50 (2005) 1–78.

[32] R. S. Mishra, Z. Y. Ma, I. Charit, Friction stir processing: a novel technique for fabrication of surface composite, Mater. Sci. Eng. A 341 (2003) 307–310.

[33] Z. Y. Ma, Friction stir processing technology: a review, Metall. Mater. Trans. A 39 (2008) 642–658.

[34] H. Rana, V. Badheka, Influence of friction stir processing conditions on the manufacturing of Al-Mg-Zn-Cu alloy/boron carbide surface composite, J. Mater. Process. Technol. 255 (2018) 795–807.

[35] N. Gangil, S. Maheshwari, E. A. Nasr, A. M. El-Tamimi, M. A. El-Meligy, A. N. Siddiquee, Another approach to characterize particle distribution during surface composite fabrication using friction stir processing, Metals 8 (2018) 568.

[36] C. Jonckheere, B. de Meester, A. Denquin, A. Simar, Torque, temperature and hardening precipitation evolution in dissimilar friction stir welds between 6061-T6 and 2014-T6 aluminium alloys, J. Mater. Process. Technol. 213 (2013) 826–837.

[37] J. Blaber, B. Adair, A. Antoniou, Ncorr: open-source 2D digital image correlation matlab software, Exp. Mech. 55 (2015) 1105–1122.

[38] R. Rodriguez, I. Gutierrez, Correlation between nanoindentation and tensile properties: Influence of the indentation size effect, Mater. Sci. Eng. A 361 (2003) 377–384.

[39] W. C. Olivier, G. M. Pharr, An improved technique for determining hardness and elastic modulus using load and displacement sensing indentation experiments, J. Mater. Res. 7 (1992) 1564–1583.

[40] J. Wang, P. D. Lee, R. W. Hamilton, M. Li, J. Allison, The kinetics of Fe-rich intermetallic formation in aluminium alloys: In situ observation, Scr. Mater. 60 (2009) 516–519.

[41] F. Hannard, S. Castin, E. Maire, R. Mokso, T. Pardoen, A. Simar, Ductilization of aluminium alloy 6056 by friction stir processing, Acta Mater. 130 (2017) 121–136.

[42] F. J. Humphreys, The thermomechanical processing of Al-SiC particlulate composites, Mater. Sci. Eng. A 135 (1991) 267–273.

[43] J. Eckert, J. C. Holzer, C. E. Krill, W. L. Johnson, Mechanically driven alloying and grain size changes in nanocrystalline Fe Cu powders, J. Appl. Phys. 73 (1993) 2794–2802.

[44] Z. F. Wu, J. Wu, L. Zhang, C. Liu, R. Wu, Solid solubility extension of copper-tin immiscible system during mechanical alloying, Mat. -wiss. u. Werkstofftech 49 (2018) 54–60.

[45] ABAQUS/Standard User's Manual, Providence, RI, 2016.

[46] H. Titrian, U. Aydin, M. Friák, D. Ma, D. Raabe, J. Neugebauer, Self-consistent scale-bridging approach to compute the elasticity of multi-phase polycrystalline materials, Mater. Res. Soc. Symp. Proc. 1524.

[47] Y. Liu, Z. Xie, J. V. Humbeeck, L. Delaey, Asymmetry of stress-strain curves under tension and compression for NiTi shape memory alloys, Acta Mater. 46 (1998) 4325–4338.

[48] F. Hannard, T. Pardoen, E. Maire, C. L. Bourlot, R. Mokso, A. Simar, Characterization and micromechanical modelling of microstructural heterogeneity effects on ductile fracture of 6xxx aluminium alloys, Acta Mater. 103 (2016) 558–572.

[49] A. Ayyar, N. Chawla, Microstructure-based modeling of the influence of particle spatial distribution and fracture on crack growth in particle-reinforced composites, Acta Mater. 55 (2007) 6064–6073.

[50] Z. G. Wei, C. Y. Tang, W. B. Lee, L. S. Cui, D. Z. Yang, Preparation of a smart composite material with TiNiCu shape memory particulates in an aluminium matrix, Mater. Lett. 32 (1997) 313–317.

[51] E. Orowan, Internal stress in metals and alloys, London: The Institute of Metals, 1948.

[52] Z. Zhang, D. L. Chen, Consideration of Orowan strengthening effect in particulate-reinforced metal matrix nanocomposites: A model for predicting their yield strength, Scr. Mater. 54 (2006) 1321–1326.

[53] V. C. Nardone, K. M. Prewo, On the strength of discontinuous silicon carbide reinforced aluminium composites, Scr. Metall. 20 (1986) 43–48.

[54] L. H. Dai, Z. Ling, Y. L. Bai, Size-dependent inelastic behavior of particle-reinforced metal-matrix composites, Compos. Sci. Technol. 61 (2001) 1057–1063.

[55] R. J. Arsenault, N. Shi, Dislocation generation due to differences between the coefficient of thermal expansion, Mater. Sci. Eng. 81 (1986) 175–187.

[56] C. Mallmann, F. Hannard, E. Ferrie, M. Fivel, R. Raudin, P. Lhuissier, A. Pacureanu, L. Salvo, A. Simar, Unveiling the impact of the effective particles distribution on strengthening mechanisms: a multiscale characterization of Mg+Y2O3 nanocomposites, Accepted in Mater. Sci. Eng. A.

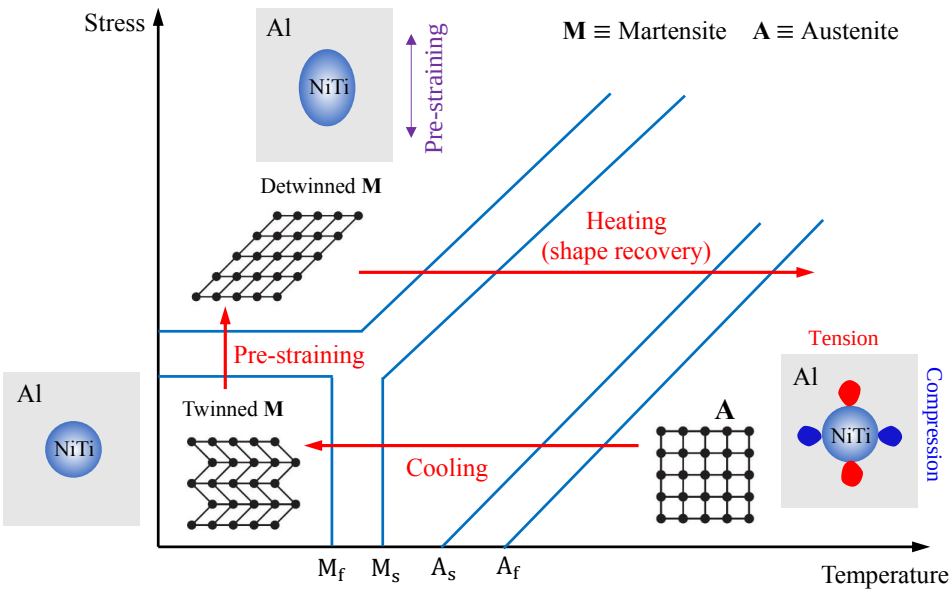

Figure 1: Design of Al/NiTi composites presenting local internal stresses. The tension (in red) and compression (in blue) fields related to the shape recovery of NiTi are drawn in the pre-straining direction (see the blue arrow in the detwinned martensite step).

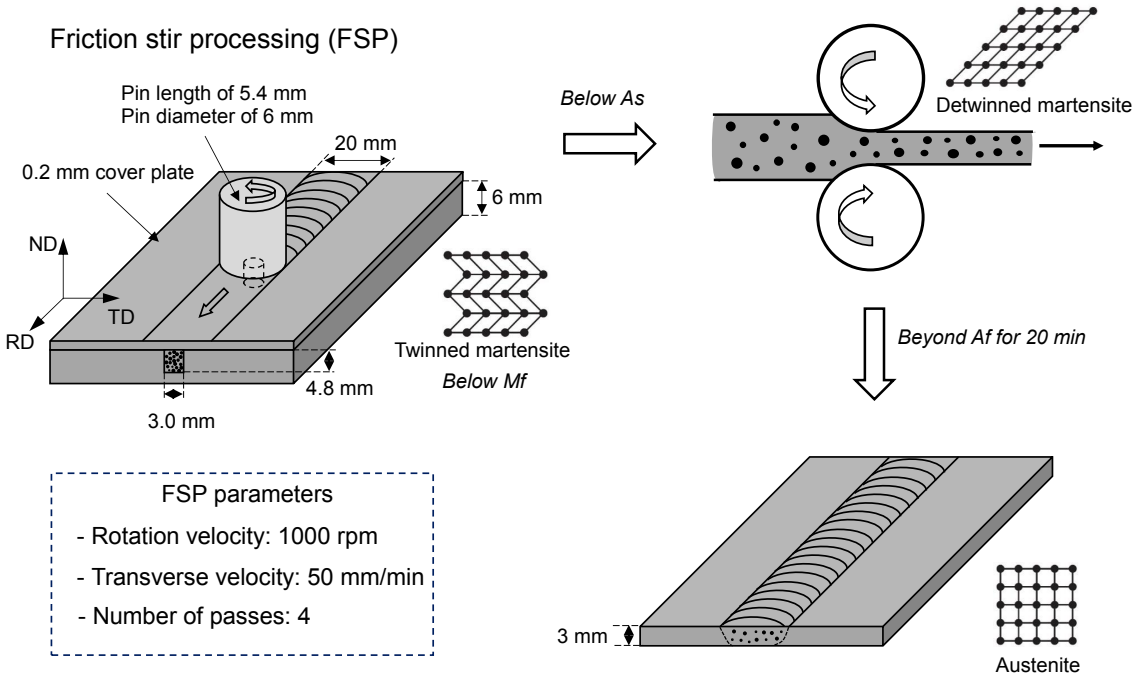

Figure 2: Sequential steps of the manufacturing of Al/NiTi composites.

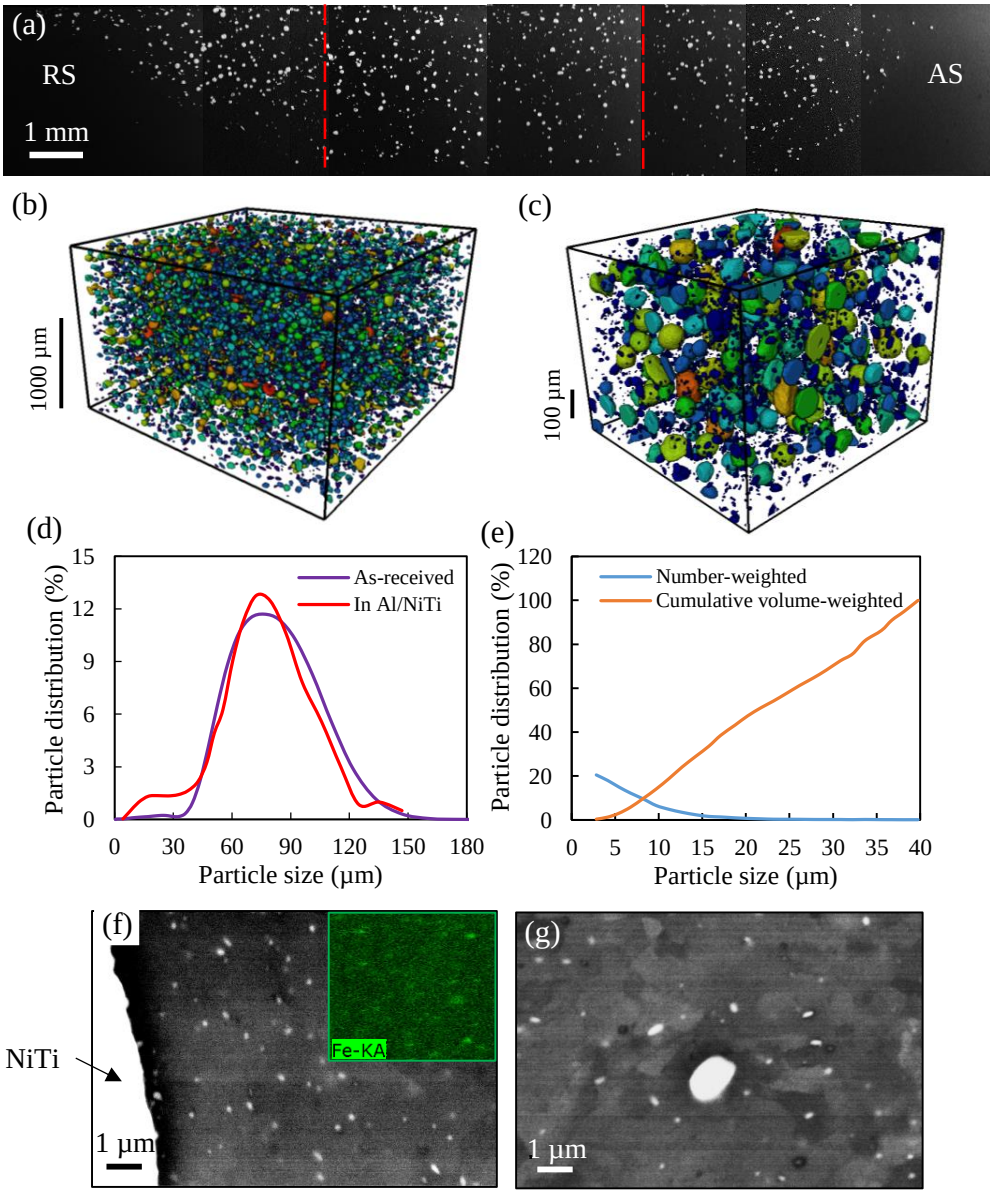

Figure 3: Distribution of NiTi particles and Fe-rich intermetallics. Overview SEM image of the friction stir processed zone (a), 3D view of NiTi particle distribution in the center of the stir zone using voxel size of 2 µm (b) and 0.8 µm (c), respectively, size distribution of both as-received powder and embedded NiTi particles (2 µm voxel size) (d), size distribution in composite for particles smaller than 40 µm (0.8 µm voxel size) (e), Fe-rich particles near the Al/NiTi interface with Fe map obtained by Energy Dispersive X-ray (EDX) analysis (f), Fe-rich particles in the friction stir processed zone in FSPed Al (g). The two red dashed lines in (a) identify the stir zone of FSP, the colors in (b) and (c) help to distinguish different particles.

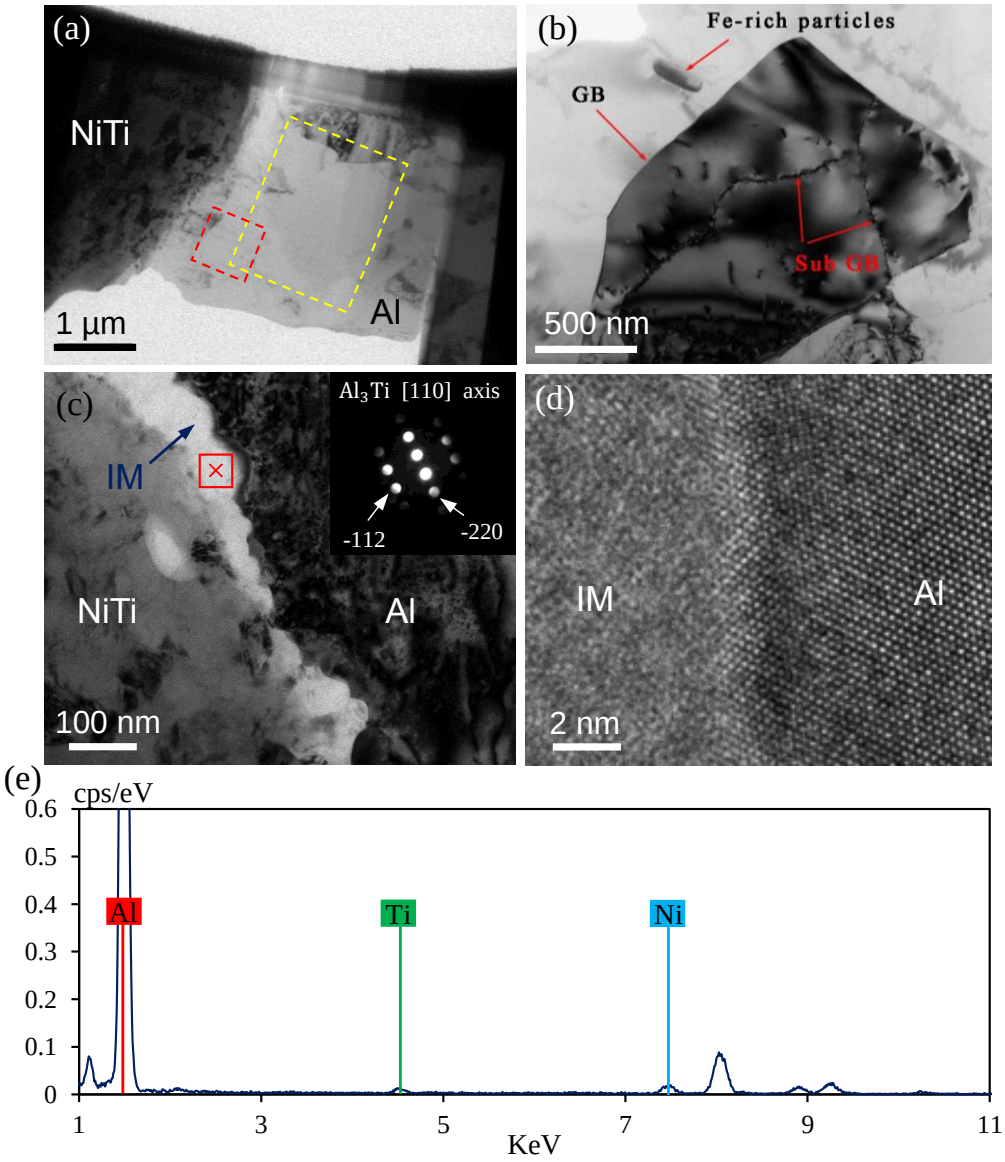

Figure 4: TEM characterization on the Al/NiTi interface. BF-TEM low magnification image of the FIB foil prepared on the interface (a), BF-TEM image showing one Al grain with sub-grain boundaries as well as Fe-rich particle in the Al matrix (b), BF-TEM image showing the intermetallic phase (see Table 3) at the Al/NiTi interface (c), high-resolution TEM revealing the atomic bonding between intermetallic and the Al matrix (d), TEM-EDX spectrum corresponding to the red box area in (a) (e). The image in (b) corresponds to the area in yellow dashed box in (a), TEM-EDX analyses in Table 3 are carried out in the red dashed box in (a) as well as the intermetallic layer in (c). The inset diffration pattern in (c) is obtained from the region indicated by the red cross.

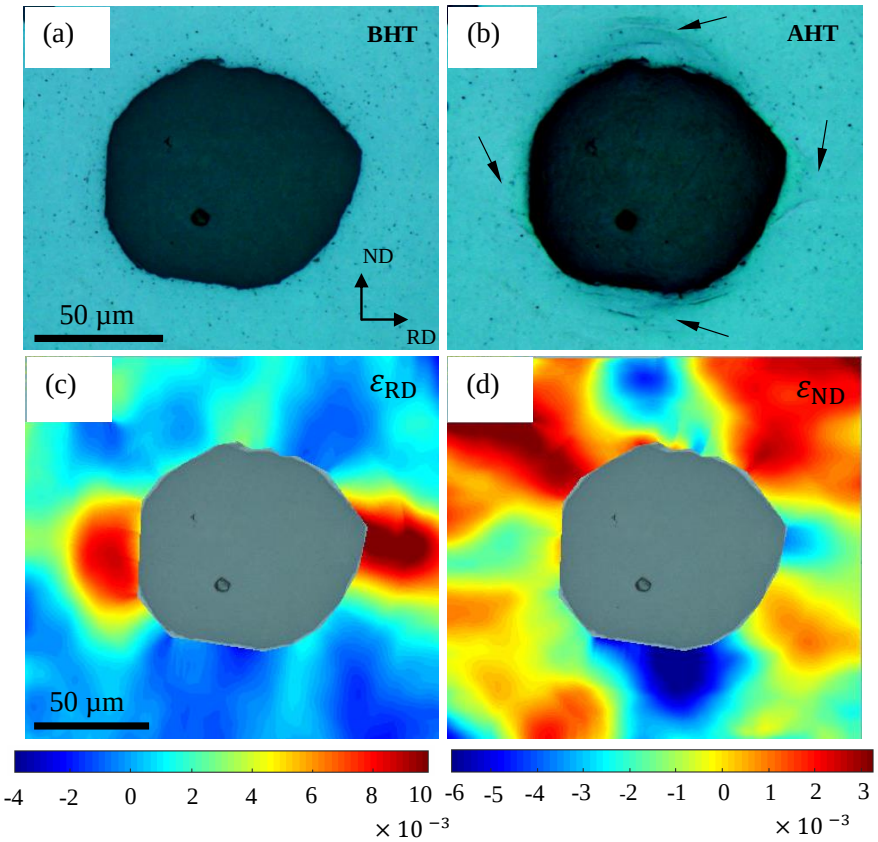

Figure 5: Detection of the shape memory effect of NiTi and evaluation of its related internal strain in the composite. Micrograph of a NiTi particle before heat treatment (BHT) (a) and after heat treatment (AHT) (b), where the arrows point out the deformation bands in the vicinity of the NiTi particle, internal strain field in the cold rolling direction (RD) (c) and internal strain field in the normal direction (ND) around the NiTi particle (d).

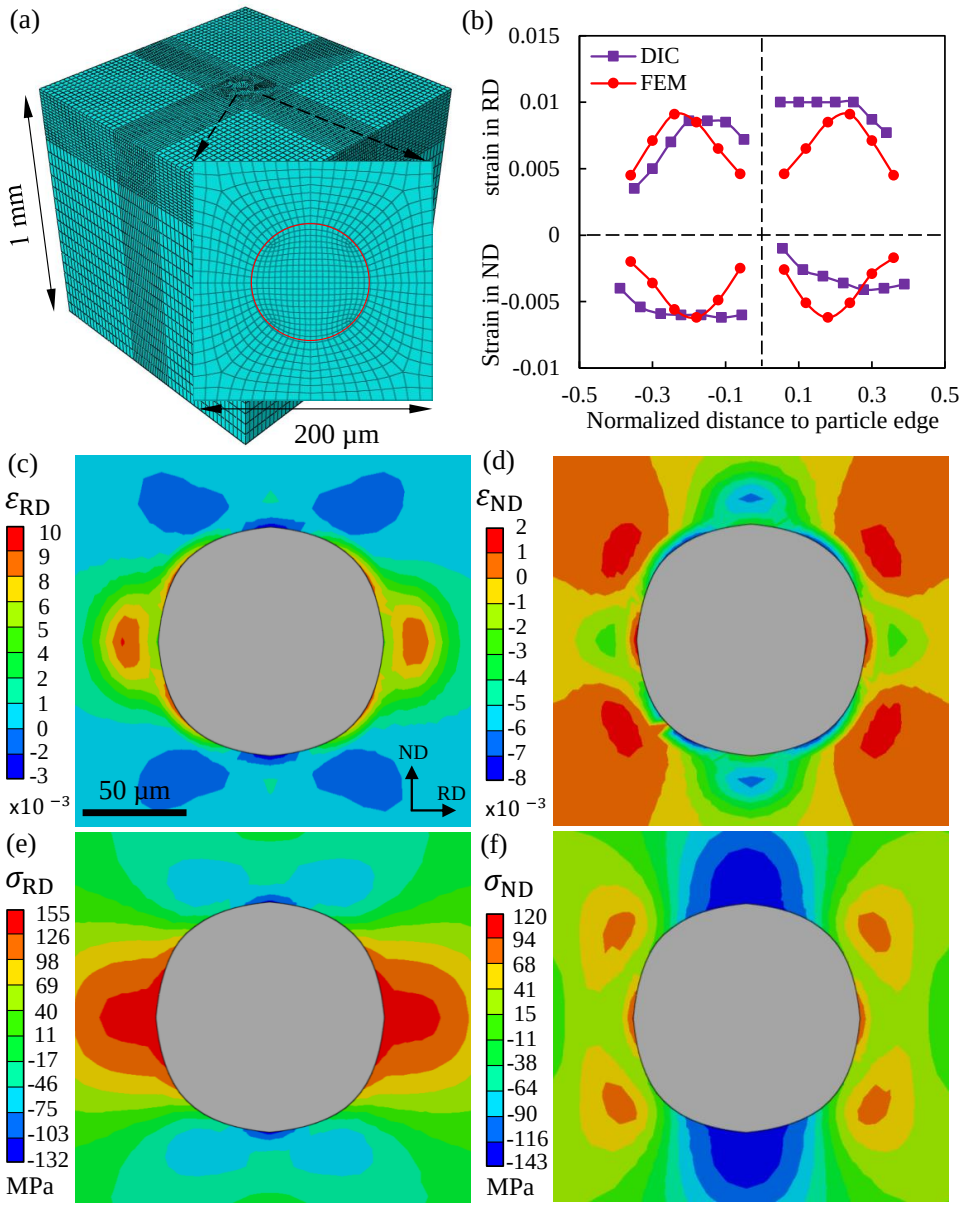

Figure 6: Finite element simulation mimicking the shape recovery of NiTi particle. The model geometry incorporating the mesh (a), comparison of strain values between the DIC measurement and the simulation result (b), plastic strain field in the cold rolling direction (RD) and perpendicular direction (ND) (c) and (d), internal stress field in the two corresponding directions (e) and (f). The red circle in (c) highlights the NiTi particle. The horizontal and vertical dashed lines in (b) represent the two edges in the RD and the two edges in the ND of the NiTi particle, respectively.

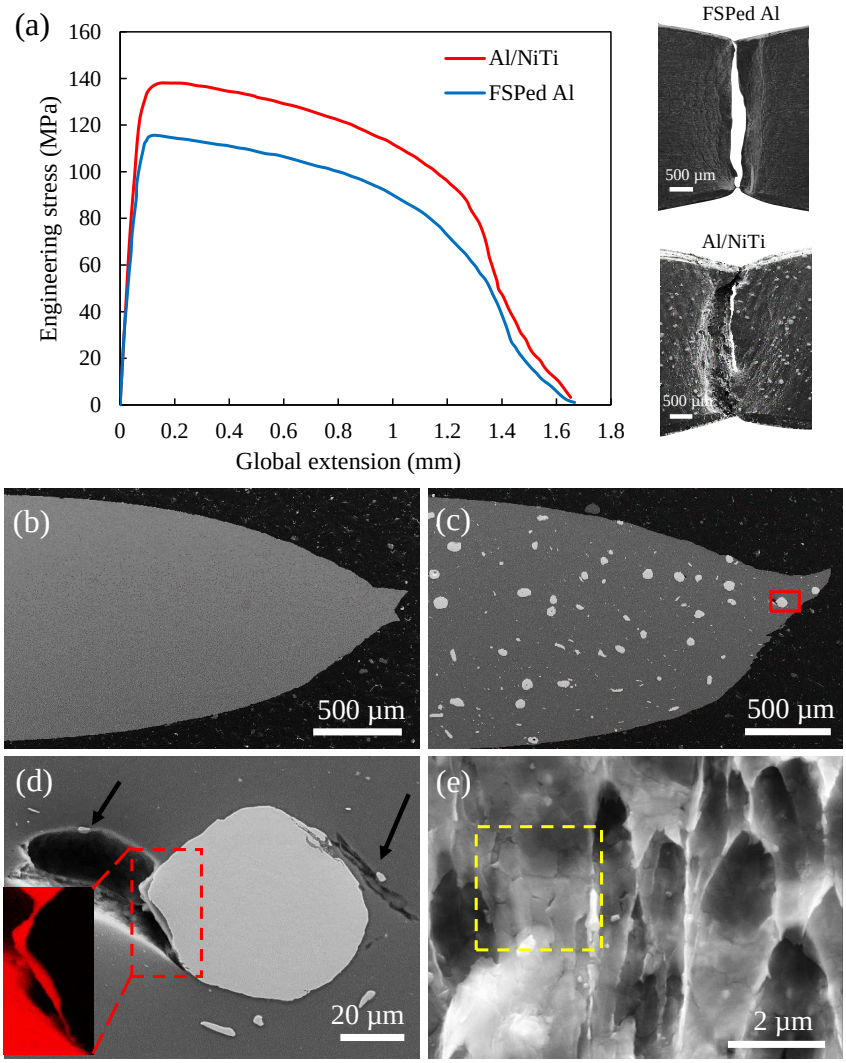

Figure 7: Tensile curve and fracture characteristics in uni-axial tensile tests. Loading curves for both Al/NiTi composite and FSPed Al (a), cross-sections revealing the fracture surface orientation for FSPed Al (b) and Al/NiTi composite (c), local damage around the NiTi particle near the fracture surface (d), and shear dimples on the fracture surface of Al/NiTi composite (e). The inset in (d) is the SEM-EDX map (Al in red) at the location of the red dashed box. The yellow dashed box in (e) highlights the sheared grains on the fracture surface.

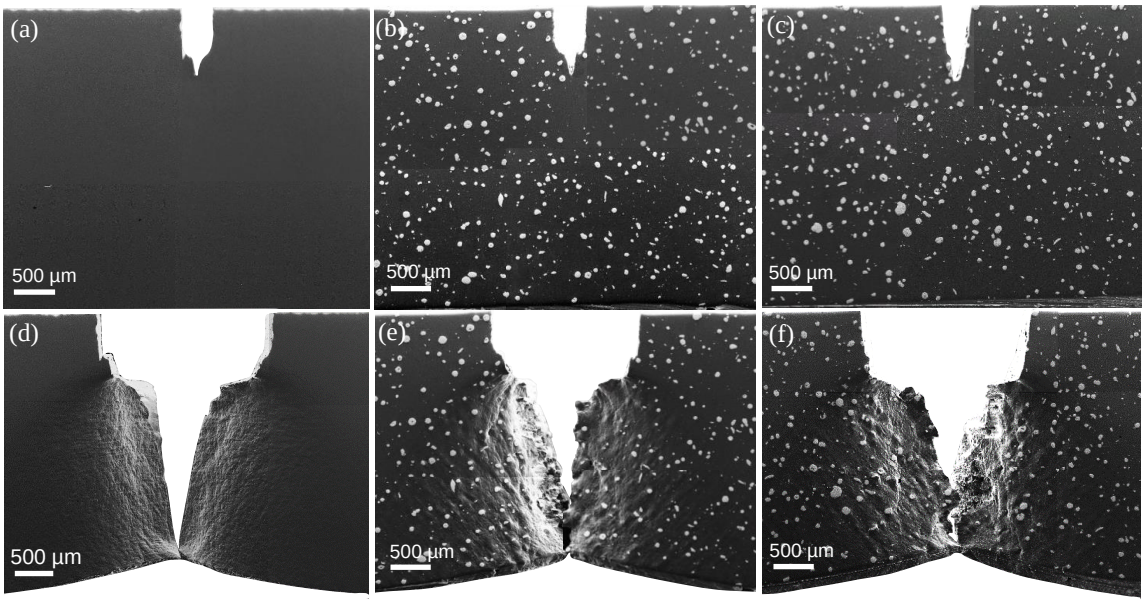

Figure 8: In-situ SEM pre-cracked tension tests. Snapshots of the samples of FSPed Al, Al/NiTi-A and Al/NiTi before loading (a)-(c), fracture paths after complete separation (d)-(f).

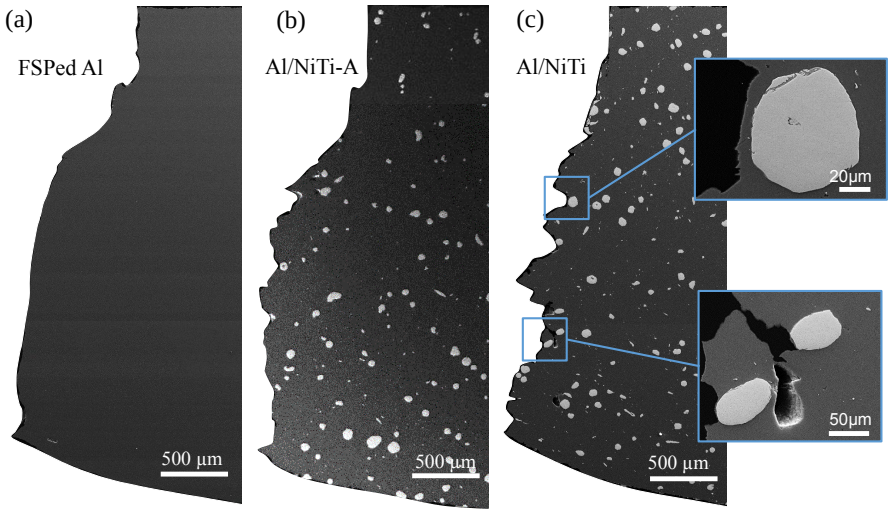

Figure 9: Fracture paths at the mid-thickness level. Overviews of the fracture path for FSPed Al (a), Al/NiTi-A (b) and Al/NiTi composite (c).

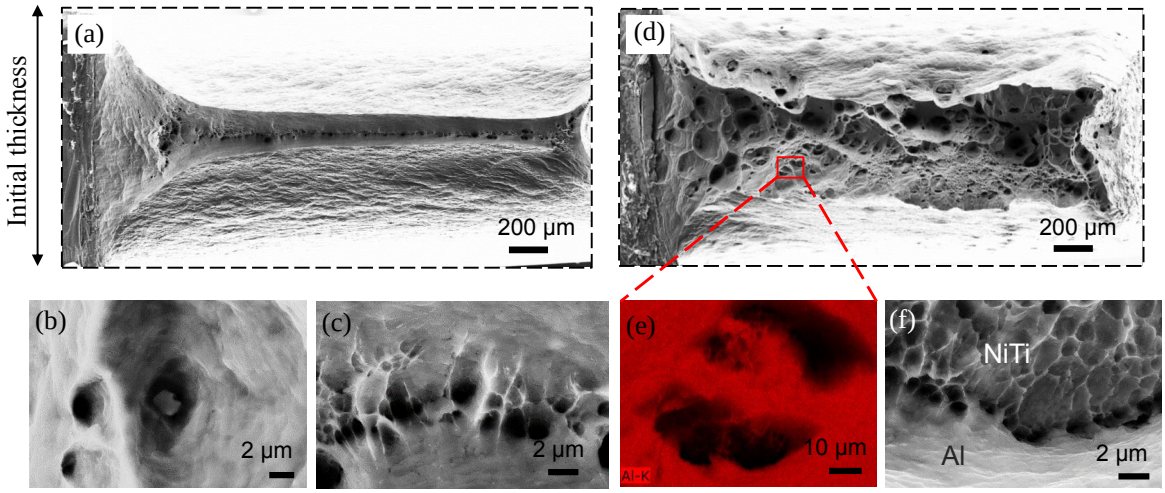

Figure 10: Fracture surface analysis. Overview of the fracture surface morphology for FSPed Al (a) and corresponding local dimple features (b) and (c), overview of the fracture surface morphology for Al/NiTi composite (d), SEM-EDX map showing the presence of Al layer on NiTi particle (e), local dimples on the Al layer covering the NiTi particle (f). The dashed lines in (a) and (d) represent the initial cross section of the sample.

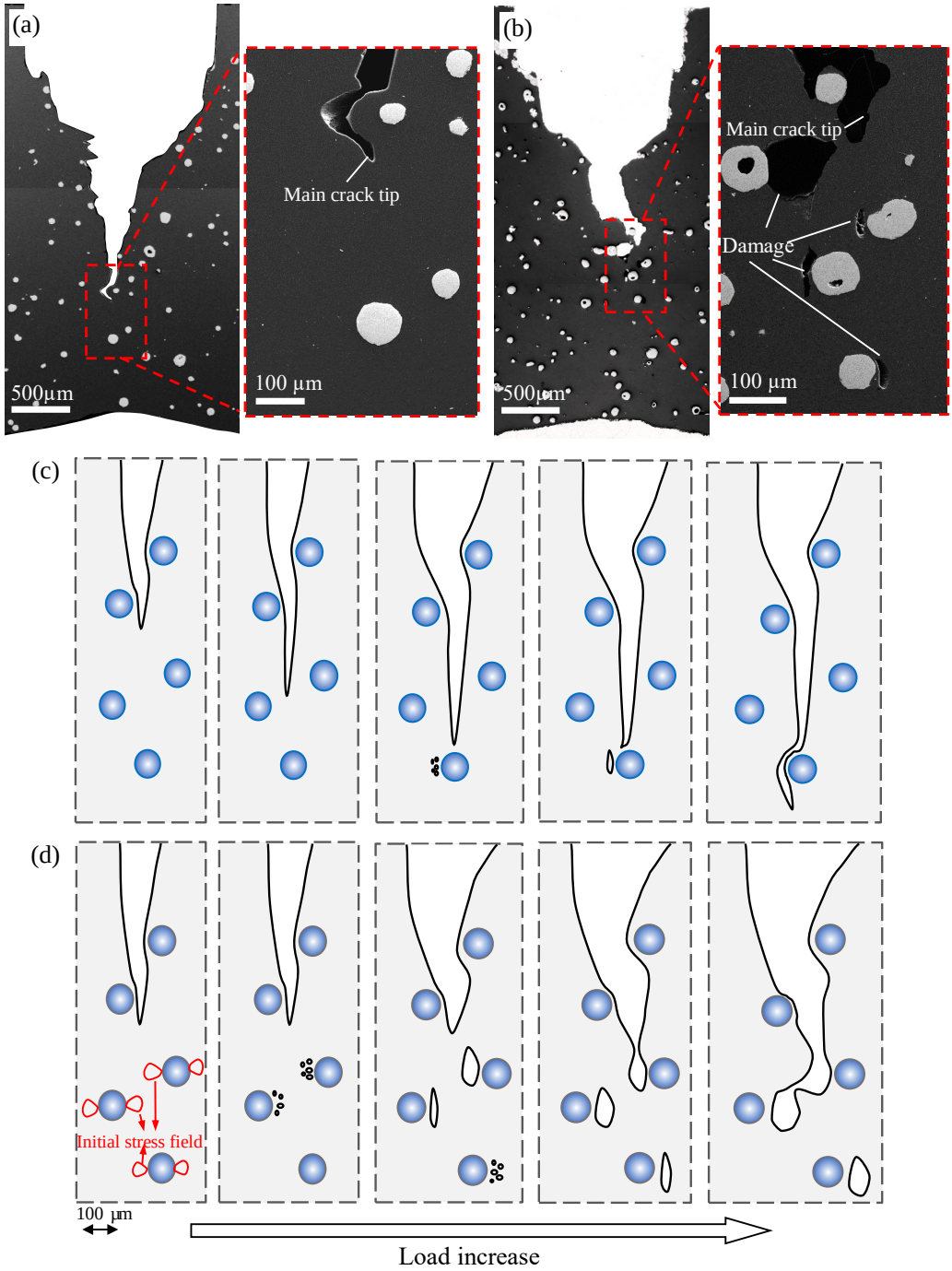

Figure 11: Elucidation of the crack deviation in composite material. Interrupted test with crack path observation on the mid-thickness plane in Al/NiTi-A (a) and Al/NiTi (b), proposed crack deviation scenarios without (c) and with initial internal stresses in the composites (d).

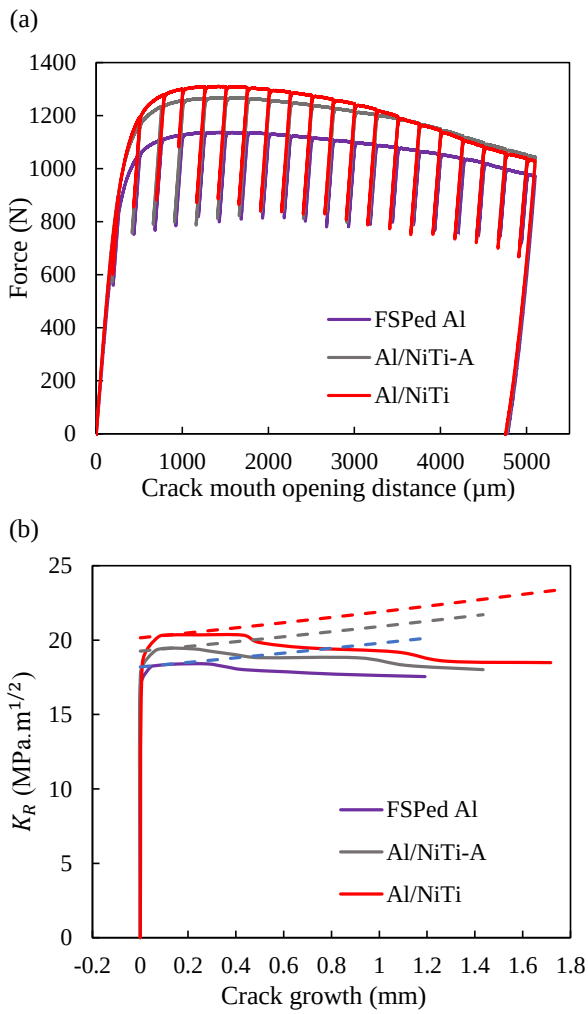

Figure 12: Compact tension tests on the Al/NiTi composite as well as the Al/NiTi-A and the FSPed Al reference materials. Loading curves incorporating the unloading history (a), K_R curves showing the plane stress fracture toughness (b).

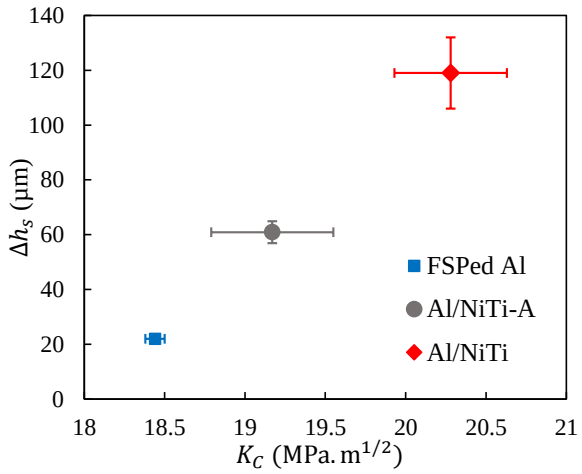

Figure 13: Correlation between fracture toughness and fracture surface roughness.

Table 1: Chemical composition of the used Al1050 (main elements).

	Al	Cu	Fe	Ga	Mg	Mn	Si
wt.%	99.5	0.01	0.21	0.01	0.03	0.03	0.02

Table 2: Al/NiTi composite and two reference materials.

Designation	FSP	Cooling to -20°C	Cold rolling	80°C HT
FSPed Al	yes	no	yes	no
Al/NiTi-A	yes	no	yes	no
Al/NiTi	yes	yes	yes	yes

Table 3: Chemical composition of regions presented in Figs. 4a and c based on TEM EDX analysis.

	Al (at. %)	Ni (at. %)	Ti (at. %)
IM	75.86	0.94	23.19
Red box	98.63	0.81	0.30

Table 4: Nanoindentation hardness and tensile properties of the FSPed Al and the Al/NiTi composite. The tensile properties are obtained from 3 specimens for each material.

	Al matrix hardness (GPa)	UTS (MPa)	ε_f
FSPed Al	0.76 ± 0.04	115 ± 2	2.56 ± 0.02
Al/NiTi	0.77 ± 0.04	139 ± 14	1.76 ± 0.15